Mode 1 drive asymmetry in inertial confinement fusion implosions on the National Ignition Facility

B. K. Spears, M. J. Edwards, S. Hatchett, J. Kilkenny, J. Knauer, A. Kritcher, J. Lindl, D. Munro, P. Patel, H. F. Robey, R. P. J. Town

December 17, 2013

Disclaimer

This document was prepared as an account of work sponsored by an agency of the United States government. Neither the United States government nor Lawrence Livermore National Security, LLC, nor any of their employees makes any warranty, expressed or implied, or assumes any legal liability or responsibility for the accuracy, completeness, or usefulness of any information, apparatus, product, or process disclosed, or represents that its use would not infringe privately owned rights. Reference herein to any specific commercial product, process, or service by trade name, trademark, manufacturer, or otherwise does not necessarily constitute or imply its endorsement, recommendation, or favoring by the United States government or Lawrence Livermore National Security, LLC. The views and opinions of authors expressed herein do not necessarily state or reflect those of the United States government or Lawrence Livermore National Security, LLC, and shall not be used for advertising or product endorsement purposes.

Mode 1 drive asymmetry in inertial confinement fusion implosions on the National Ignition Facility

Brian K. Spears,[1, *] M. J. Edwards,[1] S. Hatchett,[1] J. Kilkenny,[1] J. Knauer,[1]
A. Kritcher,[1] J. Lindl,[1] D. Munro,[1] P. Patel,[1] H. F. Robey,[1] and R. P. J. Town[1]

[1]*Lawrence Livermore National Laboratory, P.O. Box 808, Livermore, California 94551-0808, USA*

Mode 1 radiation drive asymmetry (pole-to-pole imbalance) at significant levels can have a large impact on inertial confinement fusion (ICF) implosions at the National Ignition Facility (NIF). This asymmetry distorts the cold confining shell and drives a high-speed jet through the hot spot. The perturbed hot spot shows increased residual kinetic energy and reduced internal energy, and it achieves reduced pressure and neutron yield. The altered implosion physics manifests itself in observable diagnostic signatures, especially the neutron spectrum which can be used to measure the neutron-weighted flow velocity, apparent ion temperature, and neutron downscattering. Numerical simulations of implosions with mode 1 asymmetry show that the resultant simulated diagnostic signatures are moved toward the values observed in many NIF experiments. The diagnostic output can also be used to build a set of integrated implosion performance metrics. The metrics indicate that P_1 has a significant impact on implosion performance and must be carefully controlled in NIF implosions.

I. INTRODUCTION

In order to achieve inertial confinement fusion (ICF) ignition on the National Ignition Facility (NIF) [1], we require the implosion to have nearly spherical symmetry [2]. Implosion asymmetries disturb both the central hot spot and the confining cold fuel shell. The exact effect on the hot spot and shell depends on the wavelength of the perturbation. At the shortest wavelengths, interfacial perturbations, such as those produced by target roughness, lead to mixing driven by the Richtmyer-Meshkov [3, 4] and Rayleigh-Taylor instabilities [5, 6] that result in harmful mixing of target materials [7]. On the opposite end of the wavelength spectrum, very long wavelength perturbations disturb the base hydrodynamic flow of the implosion [8, 9]. The spectrum of perturbations is most easily described by decomposing the various physical quantities of interest into Legendre components or spherical harmonics. In this paper, we focus on mode 1 perturbations. Such an imbalance could result from non-uniform laser power, target displacement from target chamber center, or deuterium-tritium (DT) cryogenic ice layer asymmetry.

II. EFFECT OF MODE 1 PERTURBATIONS ON IMPLOSION PHYSICS

We now examine the effect of mode 1 radiation drive asymmetry on HYDRA simulations[10] of ignition implosion N120205. The simulated implosion is 2D axisymmetric, but includes the full 180 degrees of polar angle to allow for mode 1 perturbations. In this full-sphere geometry we simulate a Rev5 NIF ignition capsule [2] consisting of a plastic (CH) ablator with silicon dopant and a cryogenic deuterium-tritium (DT) ice layer. Detailed dimensions are shown in Figure II.1. The implosion is driven by a spectrally-resolved radiation source developed by the detailed modeling of NIF experiments [11]. The particular source used here has been tuned to match many of the experimental observables from the NIF experiment denoted N120205. Some key implosion performance metrics are compared for this implosion in table I. The post-shot simulation provides neutron yield and hot spot pressure that are above the experiment, while the ion temperature inferred from the neutron spectrum is lower in the simulation. The one-dimensional implosion drive is designed to match very nearly the down scattered ratio, DSR, of the experiment. Additionally, the experiment is observed to have low enough mixing of CH into the DT fuel to be classified as clean. Even in the absence of mix and following precise post-shot modeling efforts including treatment of nominal surface roughness up to mode 100, there remain discrepancies between simulated and experimental performance metrics. This provides a numerical platform for testing the extent to which a hypothesized mode 1 perturbation can drive simulated results closer to experimental ones.

Mode 1 asymmetries are applied to the capsule by shaping the radiation intensity versus polar angle. In the current case, the shape of the radiation asymmetry is described by a first-order Legendre polynomial, denoted henceforth as P_1. Thus, the radiation flux, T_r^4, varies linearly with $\cos\theta$. We will refer to the magnitude of such a perturbation by quoting the amplitude of the perturbation relative to the average, or mode 0, value P_0. To be clear, a 2% $\frac{P_1}{P_0}$ perturbation refers to a radiation flux that is 2% higher than average at the north pole, but 2% lower than average at the south pole. Thus, it is a 4% peak-to-valley modulation. We must also choose how to vary $\frac{P_1}{P_0}$ as a function of time during the radiation pulse. The radiation T_r is shown vs time for N120205-based simulations in Figure II.3.

---

*Electronic address: spears9@llnl.gov

N120205	yield [neutrons]	T_{ion} [keV]	DSR	pressure [Gbar]
experiment	5.6e14	3.4	4.3	80
spherical simulation	4.1e15	3.2	4.6	150
mode 1 simulation	1.5e15	3.4	3.7	80

Table I: Comparison of post-shot simulations and experiment N120205. Two simulations are compared, a spherical one with no capsule or radiation drive asymmetry, and an analogous simulation with a 2% $\frac{P_1}{P_0}$ radiation drive asymmetry. The mode 1 perturbation drives the ion temperature, yield, and hot spot pressure closer to the experimental values. The DSR was already driven close to the experimental value by modifying the trailing edge of time history of the post-shot radiation source (see II.3) [11]. The mode 1 perturbation, in concert with the drive modification, results in DSR value that is too low. The mode 1 perturbation alone could be sufficient to approach the observed experimental DSR without the drive history adjustment.
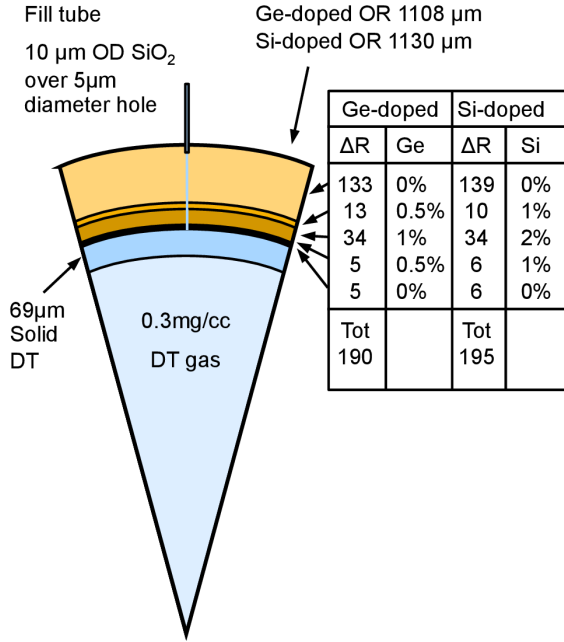

Figure II.1: Schematic of NIF ignition capsule as simulated in HYDRA. The ablator is plastic (CH) with layers of Si doping. The fuel layer is solid DT.

Figure II.2: Radiation flux asymmetry versus $\cos(\theta)$. Here θ is the polar angle, with $\theta = 0$ representing the top (or north pole) of the target chamber. The 2D HYDRA simulations describe in this paper are axisymmetric about the vertical z-axis. The asymmetry shown represents a 2% $\frac{P_1}{P_0}$ perturbation.

We focus on the strongest portion of the pulse, the 4th peak.

Perturbations during the peak with P_1 angular variation lead to a net ablation pressure imbalance directed from the high T_r side toward the low side along the axis of symmetry of our numerical problem. We note that in simulated geometry, this axis corresponds to the axis of the hohlraum that produced the radiation source. However, in real-world experiments, conditions could deviate from ideal 2D conditions, allowing the mode 1 axis to take any direction in principle. The driving pressure imbalance leads to fundamental differences between the flow of the unperturbed spherical case and the P_1 case (Figure II.4). The entire (unablated) capsule accelerates along the hohlraum axis. This acceleration produces a buoyancy force on the low-density hot spot which is enclosed in the high-density, cold shell. As a result, the hot spot floats away from the high-pressure drive. A conjugate flow develops in the ablator and dense DT fuel, leading them to accumulate on the high-drive side of the implosion. At the time of peak neutron production rate
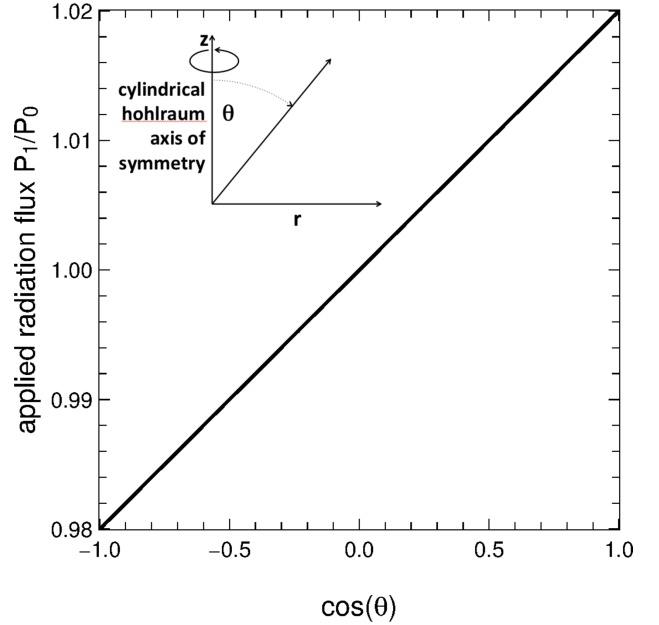
(bang time), we find that the mode-1 -driven flow produces marked angular variation of areal density, or ρR, that continues to grow through the time of peak neutron production rate, or bang time. The perturbed distribution of ion temperature, T_{ion}, and density, ρ, lead to a pressure profile that is no longer isobaric (Figure II.4, panel c), as commonly assumed in ICF models [12–15]. While the pressure is indeed slowly varying over the central hot spot, this represents only an intermediate pressure plateau. There is a relatively abrupt transition to maximum pressure upon entering the cold, dense shell on the high-drive side. This is detrimental to central hot spot implosions. The goal is to produce maximum energy density in the central hot spot to initiate a burn wave that propagates into the fuel. With the P_1 perturbation present, we have instead done considerable work on the cold fuel, leaving an underperforming hot spot. It is experimentally significant that this high pressure region is cold, and therefore produces negligible x-rays, neutrons, or other diagnostic particles. This means that diagnos-
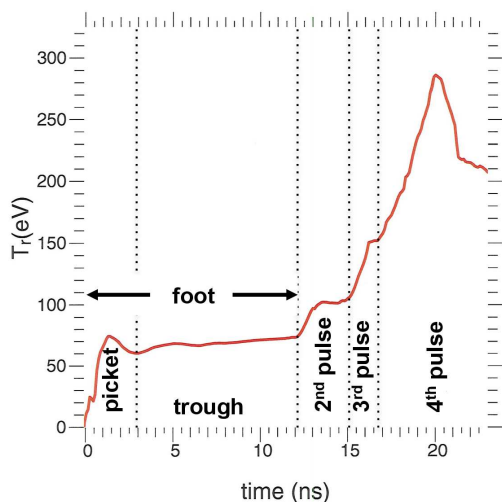
Figure II.3: The radiation time history is divided into periods associated with the launch and support of shocks. We focus here on radiation asymmetries applied during the final, 4th pulse. This pulse provides the drive for the main acceleration phase of the implosion.

tic signatures derived from particles born in the hot spot will be blind to the energy density stored in the high-pressure cold shell. It is also noteworthy that this type of perturbation reduces the pressure and the size of the hot spot to values that are consistent with experimental observations.

The hot spot evolution is further damaged by a fast-moving jet of material that propagates through the central hot spot (Figure II.5) due to the buoyancy-driven flow in the low-density center. Similar phenomena arise in bubble collapse where mode 1 symmetry can be broken by gravity-induced rise in a vertical column, [16], by collapsing near a wall [17], or by interacting with other bubbles [18, 19]. The ICF central hot spot ignition concept depends critically on the conversion of imploding shell kinetic energy into hot spot internal energy. The jet produced by mode 1 asymmetric flow represents incomplete stagnation and is therefore an appreciable loss mechanism for the hot spot. The low-density jet speed, for 2% $\frac{P_1}{P_0}$, can reach instantaneous values of $500\ km/s$. The neutron-weighted velocity is $120\ km/s$. The diagnostic significance of this neutron-emitting jet will be emphasized in section III. The physics effect of the jet is reflected in the balance of internal and kinetic energy in the hot spot at peak compression (see table II). The application of 2% P_1 results in a reduction of the hot spot internal energy to 72% of the spherical-drive value – a loss of more than 25% of the spherical-drive hot spot internal energy to unconverted kinetic energy. The residual motion also affects the apparent, average hot spot ion temperature, T_{ion}. This temperature is diagnostically inferred by measuring the Doppler broadening of the 14.028 MeV primary DT neutron peak [20, 21]. The primary peak is widened by both thermal particle motion and by continuum fluid flow, such as the jetting that results from P1 drive asymmetry. While the incomplete stagnation reduces the hot spot internal energy and the associated temper-

ature, the primary neutron peak is widened by the bulk flow. For perturbations up to 2% P1/P0, flow-based broadening overcomes the reduction of thermal temperature, leading to an increase in the apparent ion temperature. Even as the apparent ion temperature rises, the total neutron yield falls with the actual thermal temperature. A 2% P_1 results in a reduction of the simulated yield by a factor of almost 2 – from $4.5e15$ to $2.4e15$ neutrons. These sizable physics impacts affect both diagnostic signatures (detailed in section III) and the performance metrics used to judge experimental implosion quality (section IV).

III. EFFECTS OF MODE 1 PERTURBATIONS ON DIAGNOSTIC SIGNATURES

The effects of mode 1 manifest themselves in several of the many precision x-ray and nuclear diagnostics on NIF. The P_1 perturbation has a noticeable impact on the shape of the x-ray self-emission image recorded by the equatorial Gated X-Ray Detector, or GXD ([9, 22]). The GXD camera is located at the equatorial mid-plane of the NIF target chamber. Pure P_1 perturbations produce a cold fuel assembly whose exterior is nearly round (Figure III.1). The cold fuel interior boundary and associated hot spot shows a top-bottom asymmetry with a strong P_3 component that serves as a hallmark of mode 1 perturbations. Unfortunately, this means that the cold fuel and the hot spot are not completely conformal. As an exercise, we adjust the x-ray drive to symmetrize the hot spot. First we remove the obvious P_3 component of the image by adding an oppositely signed P_3 term to the x-ray drive. This leaves a hot spot that is largely oblate. We then apply in addition an oppositely signed P_2 drive, leaving a very nearly round hot spot. At each stage, while the unwanted modal content of the x-ray image is reduced, increasing distortion is communicated to the cold fuel. The end result is a hot spot with appropriately shaped x-ray emission, but with cold fuel that is unacceptably far from ideal. Furthermore, the x-ray imaging system lacks a spatial fiducial for measuring the translational motion of the self-emission image on the scale of interest here (10 - 50 um), though such translational measurements are now being made by inflight backlit radiography on the convergent ablator (2DconA) platform [23]. Thus, for more detailed diagnosis of mode 1 effects, we turn to the nuclear particle diagnostics that complement the x-ray imaging suite.

The most powerful diagnostic for measuring mode 1 effects is the suite of neutron Time of Flight (nTOF) spectrometers. These detectors measure the temporal response of a neutron scintillator to arriving neutrons from the implosion. Neutrons born at, or scattered to, different energies arrive at the detector at different times, thereby providing a direct measurement of the neutron spectrum. Aspects of the neutron spectrum provide measurements of key physics quantities discussed below. NIF has been upgraded to have 3 nTOF spectral detectors arranged on the target chamber in a roughly orthogonal triad, two near the equatorial
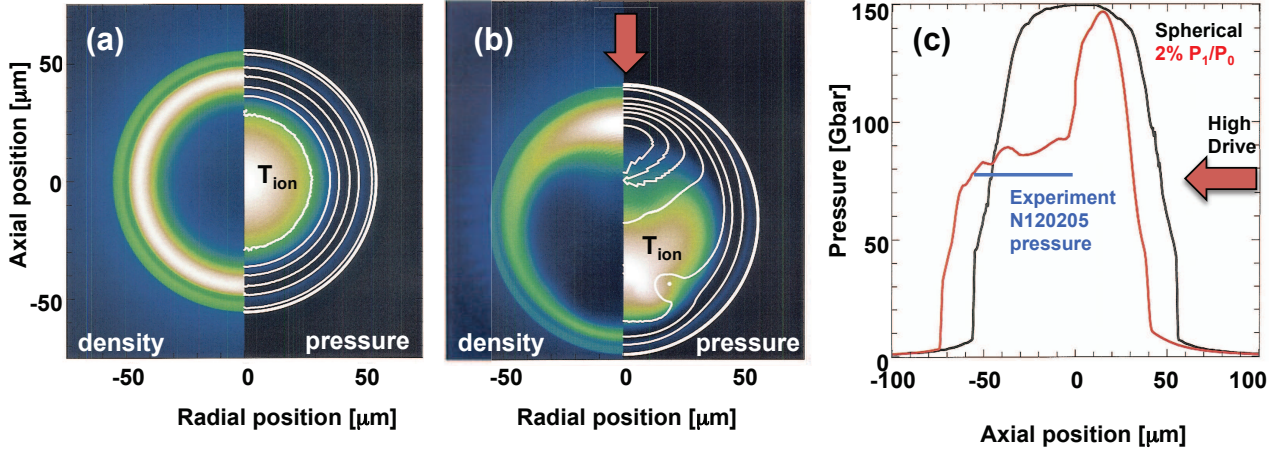
Figure II.4: comparison of symmetric and asymmetric implosions. Panel (a) symmetric implosion, panel (b) P_1-driven implosion, panel (c) pressure lineouts from both (a) and (b). Asymmetric P_1 drive alters the flow of the imploding shell and hot spot. In this case, a 2% $\frac{P_1}{P_0}$ radiation drive (high on the top in (a) and (b), on the right in (c)) leads to increased density on the high-drive side. The entire assembly translates away from the high pressure side, with the hot spot center shifted further than that of the high-density shell due to acceleration-driven buoyancy forces. The pressure profile in the hot spot and cold shell is isobaric in the symmetric case (black curve in (c)), but develops a low-pressure hot spot and high-pressure cold shell in the P_1 case.

	hot spot properties		
	internal energy [kJ]	Kinetic energy [kJ]	Apparent T_{ion} [keV]
spherical drive	5.3	0.2	3.25
2% P_1 drive	3.8	1.4	3.43

Table II: Asymmetric compression and high-speed axial jetting lead to an inefficient stagnation. The P_1 drive leads to reduced hot spot internal energy and unconverted kinetic energy. Though the internal energy is reduced, the apparent ion temperature (as inferred from the DT neutron spectral peak width) increases due to residual motion Doppler broadening.

plane and one at the bottom or south pole. The up-graded nTOF triad provides the capability to measure the neutron spectrum at enough locations to be begin to sample the angular variation of the distorted implosion.

From a mode 1 perspective, the most important measurement obtained by the nTOF suite is the neutron-weighted flow velocity. As described in section II and shown in Figure II.5, the P1-driven flow leads to very high flow velocities in the neutron emitting hot spot. This flow boosts the velocity of emitted neutrons. Consequently, fast-moving material produces fast-moving neutrons that arrive at the spectrometers earlier than their counterparts that are emitted from slow-moving material. The net flow effect is registered in the neutron spectrum as a shift in the peak energy of the neutron spectrum – to higher energies if the flow is toward the detector, to lower energies if it is away. More precisely, the neutron spectral peak represents the single component of the velocity distribution along the instrument line of sight.

The overall velocity distribution comprises both thermal and fluid velocities; while the thermal velocity distribution is isotropic for each fluid element, the fluid velocity distribution may be strongly anisotropic. The first moment of the velocity distribution shifts the peak of the observed neutron spectrum. Measurement of this shift provides a direct measurement of the flow velocity in the direction of the detector. Because the measurement is made at a nearly-orthogonal triad of locations, we can extract the complete resultant neutron-weighted velocity vector. This neutron-weighted velocity is a strong function of applied P_1, and is shown in Figure III.2. For an applied P_1/P_0 of 2%, the neutron weighted velocity is 115 $\mu m/ns$ in simulations. This represents a 50% reduction in yield relative to the unperturbed implosion. Ignition implosions on NIF require the bulk velocity to be less than 35 $\mu m/ns$. The nTOF triad reports this number with a precision of 10-30 $\mu m/ns$, making it capable of measuring the compliance of ignition implosions with specifications. Moreover, the results from the nTOF
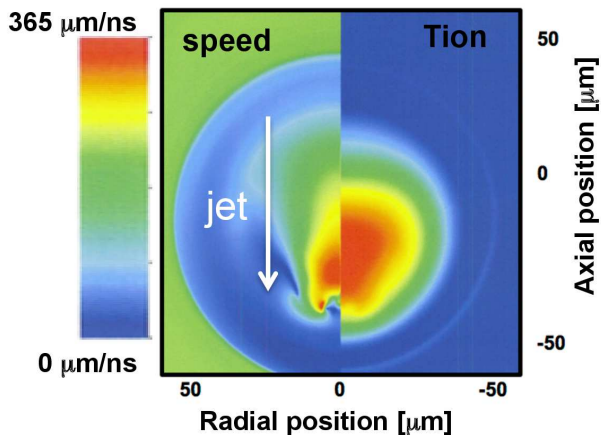
Figure II.5: Simulations show that P_1 drive asymmetry drives a strong jet of low-density fuel through the central hot spot. The kinetic energy stored in the jet represents lost internal energy in the hot spot. The jet damages the implosion, but also produces energy-shifted DT neutrons that can be observed in order to infer the flow velocity (Figure III.2).

spectrometers can be verified by comparing with the slightly less precise velocity estimates from the Magnetic Recoil Spectrometer (MRS) [24–26] .

Variations in the angular distribution of apparent ion temperature are also accessible by nTOF diagnosis. As described above (table II), flows in the hot spot due to applied P_1 alter the apparent ion temperature as inferred from the neutron spectral peak. Again, we note that the neutron spectrum represents the line-of-sight velocity distribution comprised of both thermal and fluid velocities. In contrast to the spectral peak shift introduced by non-zero first moments of the velocity distribution, the second moment broadens the neutron spectral peak. Whereas a fluid velocity distribution with non-zero first moment causes a spherical harmonic L=1 variation in spectral peak centroid shift as a function of viewing direction, a non-zero second moment causes an L=2 variation in peak width, that is, in apparent temperature, with viewing direction. For axial P_1 perturbations, this L=2 quadratic form leads to apparent temperature perturbations that are maximized at each pole, but minimized at the equator. This leads to a P_2 perturbation of ion temperature (Figure III.3). Such a distribution can potentially be observed in NIF shots and is a slightly less direct, but complementary, signature to the neutron-weighted velocity.

The nTOF spectrometers are also sensitive to angular variation in areal density of the imploding cold shell. As illustrated in Figure II.4, P_1 perturbations during the peak of the radiation drive lead to local areal density increases on the high-drive side and decreases toward the low-drive pole. To measure the areal density, the nTOFs record both the number of primary neutrons in the 13-15 MeV energy band (Y_{1315}) and the number of neutrons that have been down-scattered into the 10-12 MeV band (Y_{1012}), mainly by cold DT. Because the downscattering process scales directly with the cold shell areal

density, the down-scattered ratio, $DSR = \frac{Y_{1012}}{Y_{1315}}$, is a good measure of the areal density that has scattered neutrons into the detector line of sight. For the P1-drive case, the variation of areal density from north to south pole leads to a corresponding P_1 distribution in the DSR, shown for reference in Figure III.4. The angular distribution of DSR is dominated by a P_1 component, but shows the development of some P_2 as well. The magnitude and orientation of this DSR distribution provides another complementary diagnostic signature of mode one, albeit less direct, as many other processes (drive-induced asymmetry at other modes, hydrodynamic instability, initial target asymmetry, etc.) can alter the areal density distribution.

The diagnostic effects of velocity and areal density variation can be measured jointly by the Flange Nuclear Activation Diagnostics, or fNADS [27],[28]. This diagnostic is composed of an array of zirconium foils located at 17 locations around the target chamber. The zirconium is activated by primary neutrons born near 14 MeV from DT reactions, but it is unaffected by neutrons that downscatter off of hydrogen isotopes to energies below 12 MeV. As a result, the fNADS are sensitive to differences in primary yield as a function of angle around the target. These differences could result from anisotropy in either the emitting neutron source or in the cold scattering shell that removes neutrons from the primary peak. The Zr activation is also sensitive to effects from flow velocity. The flow shifts the neutron arrival energy to more or less sensitive regions in the Zr activation cross section. From our 2D simulations of P1 drive in the peak of the pulse, we find that the effects of primary yield variation and of flow velocity reinforce one another – they both increase the Zr activation on the low-drive side of the implosion. We produce simulated neutron spectra that are convolved with with the activation cross section for zirconium. This results in simulated zirconium yields as a function of polar angle. For spherical drive, the fNADS return a uniform signal versus angle. When P_1 drive asymmetry is present, the fNADS observe a zirconium yield that itself shows a P_1 distribution with angle. The level of P_1 observed in the fNADS scales with the level of the applied asymmetry (III.5) and is a final nuclear signature of P1 drive asymmetry.

IV. EFFECTS OF MODE 1 PERTURBATIONS ON PERFORMANCE METRICS

Having covered the detailed impacts of mode 1 perturbations on diagnostic signatures, we now turn to the gross impacts on implosion performance metrics. These metrics, constructed from average diagnostic quantities, are intended to help gauge the overall quality of an implosion. We begin with the total yield and the average apparent ion temperature, both of which are strongly affected by mode 1 perturbations. We show in Figure IV.1 the sensitivity of Tion and yield to P1 perturbations. Most notable is the dramatic yield reduction due to relatively small asymmetries.
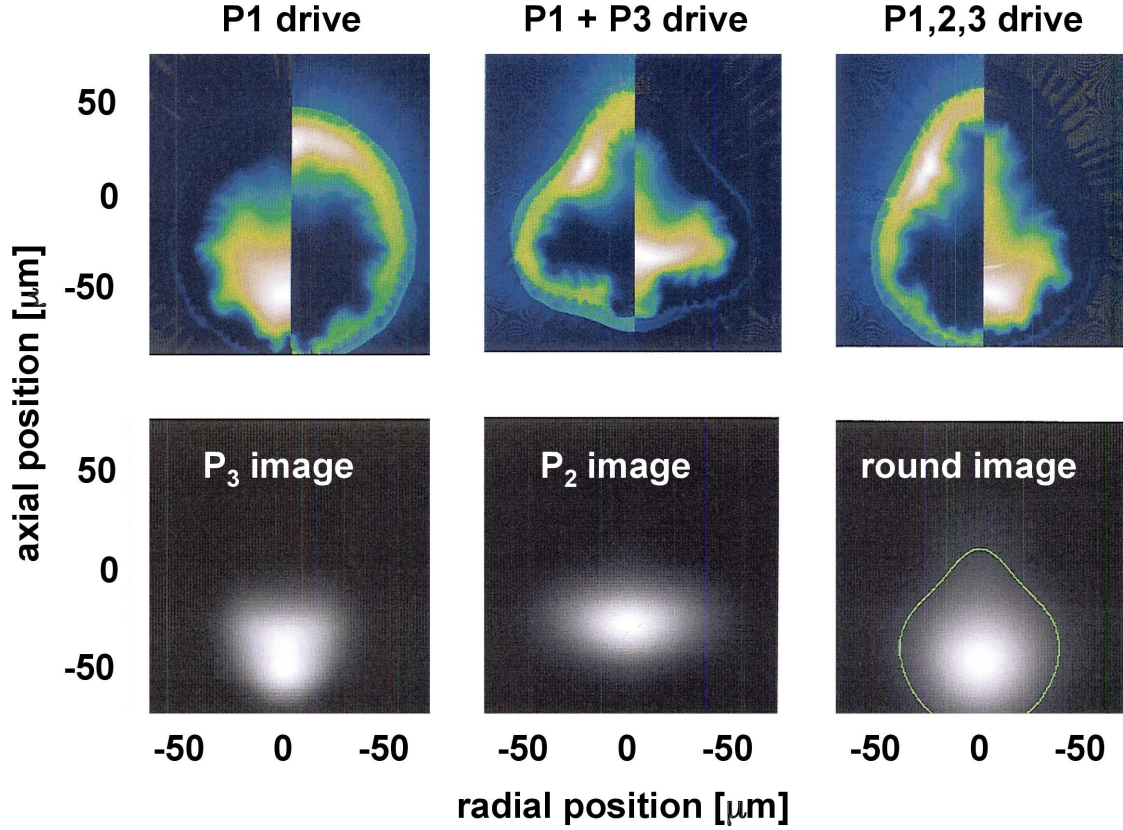
Figure III.1: comparison of density and temperature distortion with simulated x-ray images. Each image pair in a column is associated with a perturbed implosion. The top row shows density and temperature contours, while the bottom row shows the associated simulated x-ray images. In the left column, a P_1 perturbation is applied, leading to a mainly P_3 x-ray image. In the middle colum, a canceling P_3 is added to the radiation drive, leaving and oblate x-ray image. In the right column, modes 1, 2, and 3 are superposed to produce a nearly round x-ray image. While the x-ray image suggests nearly spherical symmetry, the density contour reveals that the distortion is severe. It is also noteworthy that, though a translation of nearly 40 μm is visible in the simulated images, real diagnostics at NIF have no spatial fiducial against which to measure such translations in self-emission x-ray images.

Of more interest is the correlation between the yield and the Tion. We next consider the location of an implosion in (yield,T_{ion})-space, shown in Figure IV.2. This location can be an indication of the mixing of ablator material into the hot spot ([29]), or it can indicate the presence of P1 perturbations. Here we show the trajectory traced by incrementally increasing P_1. As mentioned above, the yield falls while the apparent T_{ion} increases for P_1 perturbations less than or equal to 2%. This trajectory drives the simulated performance observables for N120205 much closer to the experiment. It is worth noting that while many hypothetical failure mechanisms (low velocity, fuel/ablator mix, etc.) result in a lowering of the yield, most also reduce the apparent ion temperature by reducing the true thermodynamic temperature of the hot spot. The P_1 mechanism is distinguished by the increase in apparent T_{ion} that results from fluid flows associated with the central hot spot jet.

This behavior is indeed distinct even from that of other low-mode perturbations. We show in Figure IV.3 similar trajectories for P_1, P_2, and P_4 over a very large perturbation range. The P_2 and P_4 trajectories reduce yield and apparent temperature for all perturbations. Eventually, even the P_1 perturbations

drag down the thermal ion temperature far enough that motion broadening cannot compensate. This highlights the competition of mechanisms for setting the apparent ion temperature. While the bulk flows within the neutron-emitting hot spot increase the apparent temperature, a mechanism that is dominant only in the P_1 simulations, loss mechanisms due to perturbations also reduce the actual thermodynamic temperature. These losses can occur by two main processes. First, the asymmetries lead to increased residual kinetic energy in the cold fuel and a reduction of the internal energy in the hot spot. Second, the perturbed interfacial region between the hot spot and the cold fuel leads to increased surface area and enhanced heat conduction, further cooling the hot spot. In the P_1 case, the increase in apparent T_{ion} driven by variance in the fluid velocity distribution dominates until the perturbation amplitude increases beyond about 2%. Beyond this, the reductions in internal energy and actual thermal T_{ion} due to incomplete stagnation and conduction dominate. In the P_2 and P_4 cases, the variance in the fluid velocity distribution is relatively small, though still weakly active in the P_2 case. The incomplete stagnation and conduction mechanisms dominate at all perturbation amplitudes
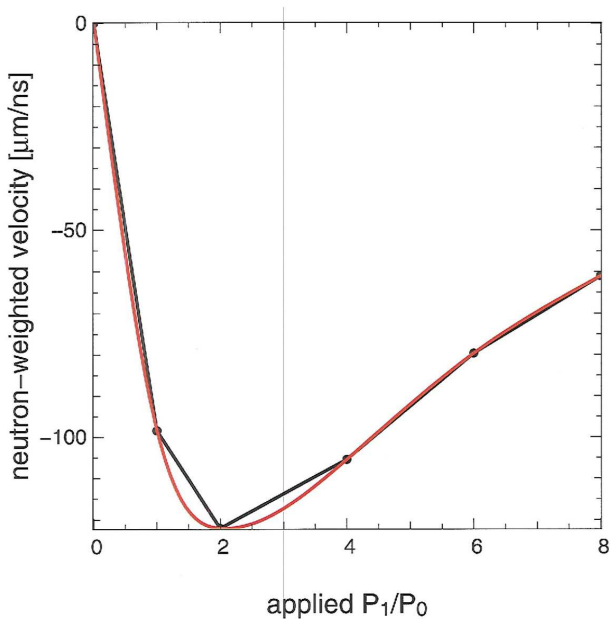
Figure III.2: Bulk velocity of the burning fuel can be measured by the NIF nuclear diagnostic suite, specifically three nearly orthogonal nTOF spectrometers and the MRS spectrometer. Neutron-weighted velocities peak near 120 km/s at perturbations of about 2 % $\frac{P_1}{P_0}$. For larger perturbations, the fast-moving, low-density hot spot jet impinges on the opposing wall of the cold shell. The neutrons produced in this jet stagnation process reduce the observed weighted velocity, though the damage to the implosion performance continues to increase with the increasing perturbation (see IV, especially Figure IV.1).

for modes 2 and 4. Eventually, all cases appear to asymptote to the same power-law trajectory as the implosion is driven to failure.

The different behaviors of the various low modes have significant implication for their interaction with one another. In Figure IV.4, we show three clusters of points. The upper gray cluster represents a collection of simulations with relatively large performance perturbations around an igniting design (with alpha heating turned off). The lower cluster represents the set of cryogenically layered implosions performed on NIF. The intermediate cluster that bridges the two represents simulations with varied amounts of modes 1 through 4. Again we see that low mode perturbations can drive the post-shot simulations toward the experimental database. When P_1 dominates, the simulations approach the experiments along the right branch. When other modes dominate, the trajectories approach via the left branch. We note that the tendency for the different modes to steer between these branches provides an ability to traverse the database of experimental performance. This is significant, as we are searching for hypotheses that move our simulations toward data in a systematic way, but also help explain the variation within the set.

The effects of mode 1 perturbations on the integrated implosion performance can best be seen in the suite of multivariate performance metrics. These metrics, discussed in detail in [30], include the ignition threshold factor (experimental), ITFX [31], the generalized Lawson criterion [30], GLC, and hot spot pressure. All three metrics effectively measure the distance between the performance of a particular implosion and the performance where an ignition cliff is reached, leading abruptly to ignition and burn. The sensitivities in Figure IV.5 indicate that mode 1 perturbations have the potential to inflict great damage on an implosion, even at relatively low asymmetry amplitudes. The metric sensitivities reinforce the notion that mode 1 perturbations must be kept below a specified level to prevent deleterious impacts to the implosion performance. For NIF implosions, the current work suggests that x-ray drive P1/P0 remain below 0.5%. This provides goal constraints on inputs to implosions, including the NIF laser power imbalance, potential power redistribution by laser-plasma interaction, and the smoothing of radiation asymmetry by the indirect drive hohlraum, as well as the symmetry of the cryogenic fuel layer. It also provides target precision for diagnostics capable of measuring the results of mode 1 perturbations.

V. CONCLUSIONS

Numerical simulations of implosions perturbed by mode 1 drive asymmetry show appreciable disturbances to the implosion hydrodynamics. The hot spot is displaced, the areal density evolves asymmetrically, and a low-density jet is driven through the hot spot. This damages the hot spot energetics, causing reduced internal energy and increased residual, wasted kinetic energy. In addition, unnecessary work is done on the high-areal-density cold fuel. This loss of energy conversion to hot spot internal energy damages the implosion, producing substantial neutron yield reduction. The effects of mode 1 perturbations appear in precision NIF diagnostics, such as gated x-ray cameras. The central hot spot x-ray image for a purely P_1-perturbed implosion is dominated by a "triangular" P_3 component. Perhaps surprisingly, combinations of mode 1, 2, and 3 perturbations can be applied to produce a nearly-spherical hot spot image while leaving unacceptably distorted cold fuel. Stronger and clearer signatures of mode 1 asymmetry are present in nuclear output from the implosion. The most direct nuclear measurements of P_1 effects come from the nearly-orthogonal triad of nTOF neutron spectrometers. The principle observable is the neutron-weighted flow velocity. This velocity, fully resolved in 3D, is a clear indication of the magnitude of P1-induced hot spot flow. Simultaneously, the nTOF instruments sample the angular variation of Tion and DSR in asymmetric implosions, the orientation of which are correlated with the neutron-weighted velocity in simulations. The fNADs provide a final nuclear-based measurement of the distribution of mode 1 asymmetry. The many diagnostic observations of mode 1 effects can be combined into a set of performance metrics to measure the impact on global implosion quality. All three metrics, ITFX, GLC, and pressure, suggest that relatively small mode 1 asymmetries can move implosions far from the ignition cliff. We thus require that P1/P0 flux perturba-
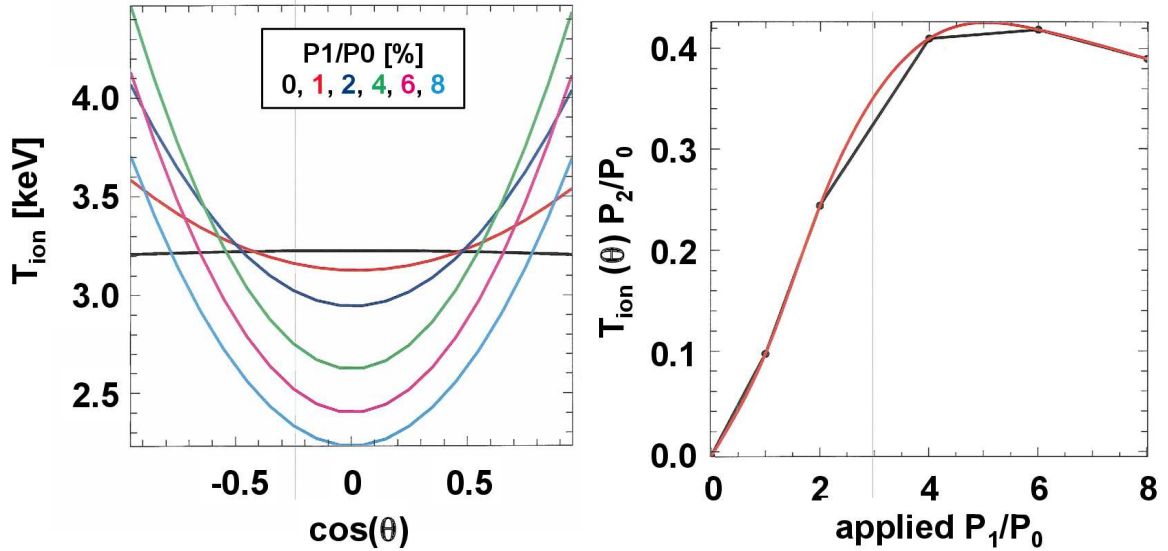
Figure III.3: Left panel: angular distribution of T_{ion} for increasing perturbation levels (black, 0%; red, 1%; blue, 2%; green, 4%; magenta, 6%; cyan, 8%). Right panel: the P_2 component of T_{ion} versus mode 1 perturbation amplitude. The jet and associate shear flow in the hot spot due to mode 1 radiation drive produces a Doppler broadening of the primary DT neutron peak that varies quadratically with $\cos(\theta)$. Because the spectral peak width is interpreted as temperature, the apparent T_{ion} is high in directions parallel (or anti-parallel) to the jet compared to directions orthogonal to the jet. The average apparent temperature falls as the perturbation increases due to real reduction in the hot spot internal energy. This can be seen clearly in the left panel by tracking the equatorial temperature at $\cos(\theta) = 0$. This direction experiences minimal broadening due to bulk flow, and consequently represents the change in the thermodynamic temperature. The amplitude of angular variation in T_{ion} increases with increasing perturbation until it approaches 0.4 (right panel).
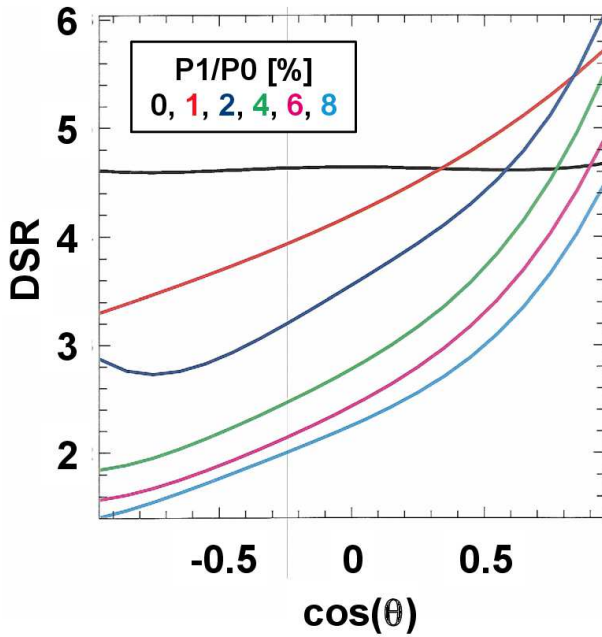

Figure III.4: P_1 perturbations result in an associated P_1 distribution of DSR with polar angle with slight higher-order contributions. Averaged over the full sphere, the DSR suffers a net decrease due to the perturbations.

tions remain small, less than 0.5%, and that diagnostics be capable of measuring the associated results, for example flow velocities of 30 km/s.

Further development of our ability to detect and understand mode 1 perturbations is underway at NIF. In addition to those already discussed, a host of existing diagnostics are being examined for their capability to measure P_1 effects, including Compton radiography, neutron imaging, and detection of charged particle asymmetries by wedge range filters (WRF). Other diagnostics and experimental platforms are being modified to enhance their relevance for mode 1 detection. These include the in-flight cold fuel x-ray imaging platform known as ConA2D, which measures the x-ray shadow cast by the cold fuel in flight. This platform has been equipped with spatial fiducials to help measure the bulk translation of the imploding shell. Modifications are also being made to the shock timing platform known as the keyhole [32, 33]. This platform uses an optical interferometer to measure shock velocities and the time at which they exit the cold fuel. The keyhole periscope is being adapted to look at both poles and the waist simultaneously to make it sensitive to the pole-to-pole drive asymmetry of mode 1 perturbations.

Most importantly, the NIF has fielded a set of experiments meant to test directly the effects of P_1 drive asymmetry on implosions. The experimental campaign includes multiple implosions of capsules without cryogenic layers but filled with DT gas (DT symcaps). These implosions were driven with an intentional and large mode 1 laser power asymmetry. Consequently, they offer a controlled level of drive perturbation that provides clear mode 1 signals to the many participating x-ray and nuclear diagnostics. These results can found in a companion paper (ref spears PRL). Later, cryogenic layered implosions will be driven with mode 1 perturbations in order to compare the effects of this low-mode asymmetry on the surrogate symcap platform and on the mainline layered platform.
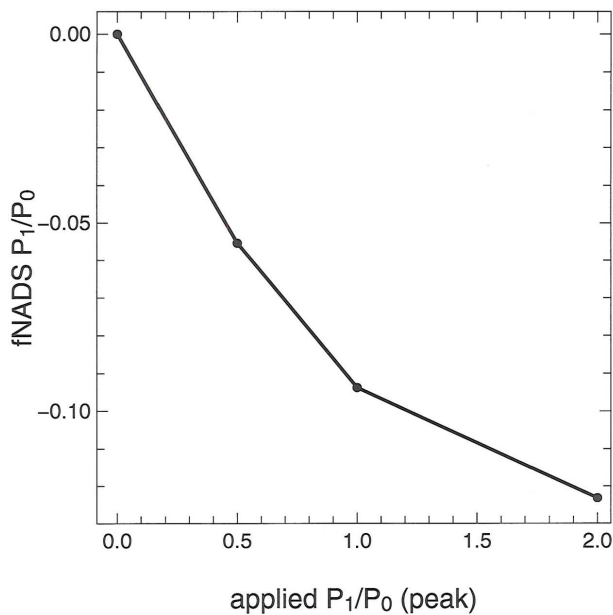
Figure III.5: fNADS Zr activation $\frac{P_1}{P_0}$. Zirconium disks are differentially activated as a function of polar angle due to an applied P_1 asymmetry. The activation is increased on the low-drive implosion side due to two reinforcing effects. First, the areal density is low on the low drive side, reducing the scatter away from the detector. Second, the net velocity shifts the neutron energies to a more sensitive band of the Zr activation cross-section. The result is a P_1 distribution of Zr activation that increases in amplitude monotonically with the applied drive perturbation.

[1] M. J. Edwards, P. K. Patel, J. D. Lindl, L. J. Atherton, S. H. Glenzer, S. W. Haan, J. D. Kilkenny, O. L. Landen, E. I. Moses, A. Nikroo, R. Petrasso, T. C. Sangster, P. T. Springer, S. Batha, R. Benedetti, L. Bernstein, R. Betti, D. L. Bleuel, T. R. Boehly, D. K. Bradley, J. A. Caggiano, D. A. Callahan, P. M. Celliers, C. J. Cerjan, K. C. Chen, D. S. Clark, G. W. Collins, E. L. Dewald, L. Divol, S. Dixit, T. Doeppner, D. H. Edgell, J. E. Fair, M. Farrell, R. J. Fortner, J. Frenje, M. G. G. Johnson, E. Giraldez, V. Y. Glebov, G. Grim, B. A. Hammel, A. V. Hamza, D. R. Harding, S. P. Hatchett, N. Hein, H. W. Herrmann, D. Hicks, D. E. Hinkel, M. Hoppe, W. W. Hsing, N. Izumi, B. Jacoby, O. S. Jones, D. Kalantar, R. Kauffman, J. L. Kline, J. P. Knauer, J. A. Koch, B. J. Kozioziemski, G. Kyrala, K. N. LaFortune, S. Le Pape, R. J. Leeper, R. Lerche, T. Ma, B. J. MacGowan, A. J. MacKinnon, A. Macphee, E. R. Mapoles, M. M. Marinak, M. Mauldin, P. W. McKenty, M. Meezan, P. A. Michel, J. Milovich, J. D. Moody, M. Moran, D. H. Munro, C. L. Olson, K. Opachich, A. E. Pak, T. Parham, H. S. Park, J. E. Ralph, S. P. Regan, B. Remington, H. Rinderknecht, H. F. Robey, M. Rosen, S. Ross, J. D. Salmonson, J. Sater, D. H. Schneider, F. H. Seguin, S. M. Sepke, D. A. Shaughnessy, V. A. Smalyuk, B. K. Spears, C. Stoeckl, W. Stoeffl, L. Suter, C. A. Thomas, R. Tommasini, R. P. Town, S. V. Weber, P. J. Wegner, K. Widman, M. Wilke, D. C. Wilson, C. B. Yeamans, and A. Zylstra, PHYSICS OF PLASMAS **20**, (2013).

[2] S. W. Haan, J. D. Lindl, D. A. Callahan, D. S. Clark, J. D. Salmonson, B. A. Hammel, L. J. Atherton, R. C. Cook, M. J. Edwards, S. Glenzer, A. V. Hamza, S. P. Hatchett, M. C. Herrmann, D. E. Hinkel, D. D. Ho, H. Huang, O. S. Jones, J. Kline, G. Kyrala, O. L. Landen, B. J. MacGowan, M. M. Marinak, D. D. Meyerhofer, J. L. Milovich, K. A. Moreno, E. I. Moses, D. H. Munro, A. Nikroo, R. E. Olson, K. Peterson, S. M. Pollaine, J. E. Ralph, H. F. Robey, B. K. Spears, P. T. Springer, L. J. Suter, C. A. Thomas, R. P. Town, R. Vesey, S. V. Weber, H. L. Wilkens, and D. C. Wilson, PHYSICS OF PLASMAS **18**, (2011).

[3] R. RICHTMYER, COMMUNICATIONS ON PURE AND APPLIED MATHEMATICS **13**, 297 (1960).

[4] E. E. Meshkov, Izv. Acad. Sci. USSR Fluid Dynamics **4**, 101 (1969).

[5] L. Rayleigh, *Scientific Papers II* (Cambridge, England, 1900).

[6] G. TAYLOR, PROCEEDINGS OF THE ROYAL SOCIETY OF LONDON SERIES A-MATHEMATICAL AND PHYSICAL SCIENCES **201**, 192 (1950).

[7] D. S. Clark, S. W. Haan, A. W. Cook, M. J. Edwards, B. A. Hammel, J. M. Koning, and M. M. Marinak, PHYSICS OF PLASMAS **18**, (2011).

[8] J. Lindl, P. Amendt, R. Berger, S. Glendinning, S. Glenzer, S. Haan, R. Kauffman, O. Landen, and L. Suter, PHYSICS OF PLASMAS **11**, 339 (2004).

[9] G. A. Kyrala, J. L. Kline, S. Dixit, S. Glenzer, D. Kalantar, D. Bradley, N. Izumi, N. Meezan, O. Landen, D. Callahan, S. V. Weber, J. P. Holder, S. Glenn, M. J. Edwards, J. Koch, L. J. Suter, S. W. Haan, R. P. J. Town, P. Michel, O. Jones, S. Langer, J. D.
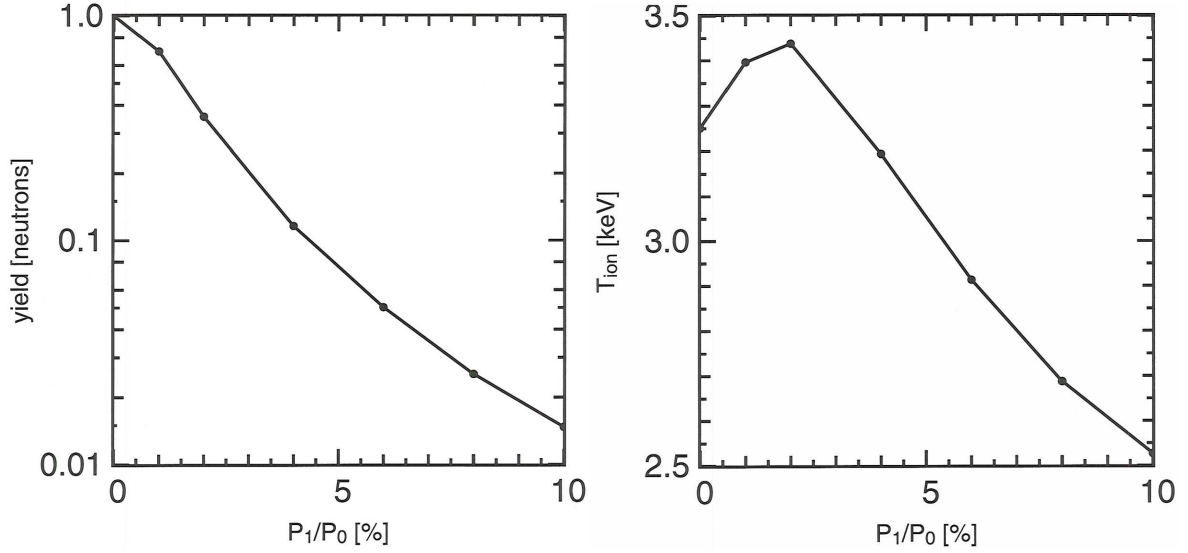
Figure IV.1: Total neutron yield is sensitive to P_1, falling a factor of 2 due to application of a 2% $\frac{P_1}{P_0}$ x-ray flux perturbation. The apparent ion temperature, observed from broadening of the primary peak in the emitted neutron spectrum, rises with increasing P_1 perturbation amplitude due to residual motion of the burning fuel up to perturbations of 2% $\frac{P_1}{P_0}$. Eventually, the internal energy is reduced enough that the decrease in the thermodynamic temperature is larger than the apparent increase due to motion broadening. Consequently, the apparent ion temperature falls at very large perturbation amplitude.
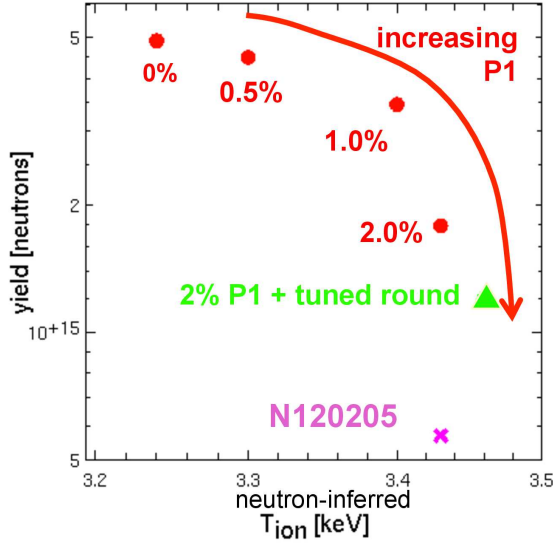

Figure IV.2: Mode 1 drive asymmetry reduces the yield, increases the T_{ion}, and drives the simulated results closer to the experimental observation. The red points represent post shot simulations of N120205 with increasing amounts of P_1 perturbation. The green point represents a post shot simulation with mode 1 radiation drive asymmetry together with modes 2, 3, and 4. The amount of each mode was chosen to produce a relatively round simulated x-ray image.
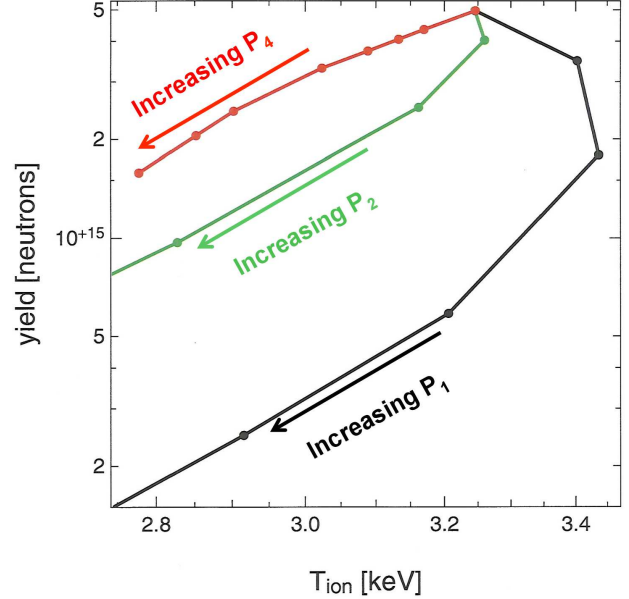

Figure IV.3: Trajectories in (yield,T_{ion})-space are different for P_1 and other low-mode disturbances. The trajectory parameterized by increasing P_1 drive asymmetry (black) illustrates the relation between the non-monotonic apparent temperature behavior and the associated yield behavior. Similar trajectories parameterized by increasing P_2 drive (green) and P_4 drive (red) show only the monotonic decrease of both yield and T_{ion} as inferred from the neutron spectrum.

Moody, E. L. Dewald, T. Ma, J. Ralph, A. Hamza, E. Dzenitis, and J. Kilkenny, PHYSICS OF PLASMAS **18**, (2011), 52nd Annual Meeting of the APS Division of Plasma Physics, Chicago, IL, 2010.

[10] M. Marinak, G. Kerbel, N. Gentile, O. Jones, D. Munro, S. Pollaine, T. Dittrich, and S. Haan, PHYSICS OF PLASMAS **8**, 2275 (2001).

[11] D. S. Clark, D. E. Hinkel, D. C. Eder, O. S. Jones,

S. W. Haan, B. A. Hammel, M. M. Marinak, J. L. Milovich, H. F. Robey, L. J. Suter, and R. P. J. Town, PHYSICS OF PLASMAS **20**, (2013).

[12] M. Rosen, J. Lindl, and A. Thiessen, Laser Program Annual Report, UCRL 50055-83 (1983).
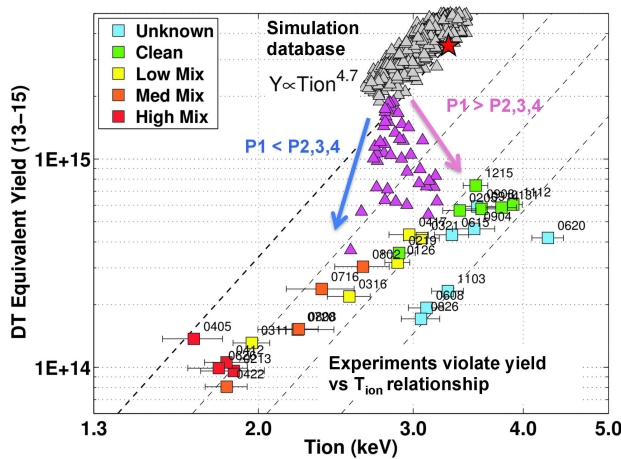
[13] M. Herrmann, M. Tabak, and J. Lindl, NUCLEAR

Figure IV.4: simulation and experiment ensembles in (yield,T_{ion})-space. The gray cloud represents simulations of low-performing Rev5 ignition implosions. The colored boxes represent experiments on NIF. The magenta triangles are associated with simulations including various amounts of low mode drive asymmetry. The interaction of modes 1 through 4 allow us to steer the simulated points toward the experimental data. While the yield is always reduced, the ability of mode 1 perturbations to increase the apparent ion temperature can be exploited to adjust both the temperature and yield in a way that makes contact with the experimental database.

FUSION **41**, 99 (2001).

[14] C. D. Zhou and R. Betti, PHYSICS OF PLASMAS **14**, (2007).

[15] J. MEYERTERVEHN, NUCLEAR FUSION **22**, 561 (1982).

[16] J. H. W.Z. Li, Y.Y. Yan, International Journal of Numerical Methods for Heat and Fluid Flow **13**, 940 (2003).

[17] S. ZHANG and J. DUNCAN, PHYSICS OF FLUIDS **6**, 2352 (1994).

[18] Y.-H. Chen and I. Lin, PHYSICAL REVIEW E **77**, (2008).

[19] A. Pain, B. H. T. Goh, E. Klaseboer, S.-W. Ohl, and B. C. Khoo, JOURNAL OF APPLIED PHYSICS **111**, (2012).

[20] H. BRYSK, PLASMA PHYSICS AND CONTROLLED FUSION **15**, 611 (1973).

[21] L. Ballabio, J. Kallne, and G. Gorini, NUCLEAR FUSION **38**, 1723 (1998).

[22] R. Town, PHYSICS OF PLASMAS (submitted, December 2013).

[23] R. Rygg, PHYSICS REVIEW LETTERS (submitted, November 2013).

[24] M. G. Johnson, D. T. Casey, J. A. Frenje, C.-K. Li, F. H. Seguin, R. D. Petrasso, R. Ashabranner, R. Bionta, S. LePape, M. McKernan, A. Mackinnon, J. D. Kilkenny, J. Knauer, and T. C. Sangster, PHYSICS OF PLASMAS **20**, (2013).

[25] J. A. Frenje, D. T. Casey, C. K. Li, F. H. Seguin, R. D. Petrasso, V. Y. Glebov, P. B. Radha, T. C. Sangster, D. D. Meyerhofer, S. P. Hatchett, S. W. Haan, C. J. Cerjan, O. L. Landen, K. A. Fletcher, and R. J. Leeper, PHYSICS OF PLASMAS **17**, (2010), 51st Annual Meeting of the Division-of-Plasma-Physics of the American-Physics-Society, Atlanta, GA, NOV 02-06, 2009.

[26] D. T. Casey, J. A. Frenje, F. H. Seguin, C. K. Li, M. J. Rosenberg, H. Rinderknecht, M. J. E. Manuel, M. G. Johnson, J. C. Schaeffer, R. Frankel, N. Sinenian, R. A. Childs, R. D. Petrasso, V. Y. Glebov, T. C. Sangster, M. Burke, and S. Roberts, REVIEW OF SCIENTIFIC INSTRUMENTS **82**, (2011).

[27] D. L. Bleuel, C. B. Yeamans, L. A. Bernstein, R. M. Bionta, J. A. Caggiano, D. T. Casey, G. W. Cooper, O. B. Drury, J. A. Frenje, C. A. Hagmann, R. Hatarik, J. P. Knauer, M. G. Johnson, K. M. Knittel, R. J. Leeper, J. M. McNaney, M. Moran, C. L. Ruiz, and D. H. G. Schneider, REVIEW OF SCIENTIFIC INSTRUMENTS **83**, (2012), 19th Topical Conference on High-Temperature Plasma Diagnostics, Monterey, CA, MAY 06-10, 2012.

[28] C. B. Yeamans, D. L. Bleuel, and L. A. Bernstein, REVIEW OF SCIENTIFIC INSTRUMENTS **83**, (2012), 19th Topical Conference on High-Temperature Plasma Diagnostics, Monterey, CA, MAY 06-10, 2012.

[29] T. Ma, P. K. Patel, N. Izumi, P. T. Springer, M. H. Key, L. J. Atherton, L. R. Benedetti, D. K. Bradley, D. A. Callahan, P. M. Celliers, C. J. Cerjan, D. S. Clark, E. L. Dewald, S. N. Dixit, T. Doeppner, D. H. Edgell, R. Epstein, S. Glenn, G. Grim, S. W. Haan, B. A. Hammel, D. Hicks, W. W. Hsing, O. S. Jones, S. F. Khan, J. D. Kilkenny, J. L. Kline, G. A. Kyrala, O. L. Landen, S. Le Pape, B. J. MacGowan, A. J. Mackinnon, A. G. MacPhee, N. B. Meezan, J. D. Moody, A. Pak, T. Parham, H. S. Park, J. E. Ralph, S. P. Regan, B. A. Remington, H. F. Robey, J. S. Ross, B. K. Spears, V. Smalyuk, L. J. Suter, R. Tommasini, R. P. Town, S. V. Weber, J. D. Lindl, M. J. Edwards, S. H. Glenzer, and E. I. Moses, PHYSICAL REVIEW LETTERS **111**, (2013).

[30] B. K. Spears, S. Glenzer, M. J. Edwards, S. Brandon, D. Clark, R. Town, C. Cerjan, R. Dylla-Spears, E. Mapoles, D. Munro, J. Salmonson, S. Sepke, S. Weber, S. Hatchett, S. Haan, P. Springer, E. Moses, J. Kline, G. Kyrala, and D. Wilson, PHYSICS OF PLASMAS **19**, (2012).

[31] B. K. Spears, S. Brandon, D. Clark, C. Cerjan, J. Edwards, O. Landen, J. Lindl, S. Haan, S. Hatchett, J. Salmonson, P. Springer, S. V. Weber, and D. Wilson, Journal of Physics: Conference Series **244**, 022014 (2010).

[32] H. F. Robey, P. M. Celliers, J. L. Kline, A. J. Mackinnon, T. R. Boehly, O. L. Landen, J. H. Eggert, D. Hicks, S. Le Pape, D. R. Farley, M. W. Bowers, K. G. Krauter, D. H. Munro, O. S. Jones, J. L. Milovich, D. Clark, B. K. Spears, R. P. J. Town, S. W. Haan, S. Dixit, M. B. Schneider, E. L. Dewald, K. Widmann, J. D. Moody, T. D. Doeppner, H. B. Radousky, A. Nikroo, J. J. Kroll, A. V. Hamza, J. B. Horner, S. D. Bhandarkar, E. Dzenitis, E. Alger, E. Giraldez, C. Castro, K. Moreno, C. Haynam, K. N. LaFortune, C. Widmayer, M. Shaw, K. Jancaitis, T. Parham, D. M. Holunga, C. F. Walters, B. Haid, T. Malsbury, D. Trummer, K. R. Coffee, B. Burr, L. V. Berzins, C. Choate, S. J. Brereton, S. Azevedo, H. Chandrasekaran, S. Glenzer, J. A. Caggiano, J. P. Knauer, J. A. Frenje, D. T. Casey, M. G. Johnson, F. H. Seguin, B. K. Young, M. J. Edwards, B. M. Van Wonterghem, J. Kilkenny, B. J. MacGowan, J. Atherton, J. D. Lindl, D. D. Meyerhofer, and E. Moses, PHYSICAL REVIEW LETTERS **108**, (2012).

[33] H. F. Robey, T. R. Boehly, P. M. Celliers, J. H. Eggert, D. Hicks, R. F. Smith, R. Collins, M. W. Bowers, K. G. Krauter, P. S. Datte, D. H. Munro, J. L.
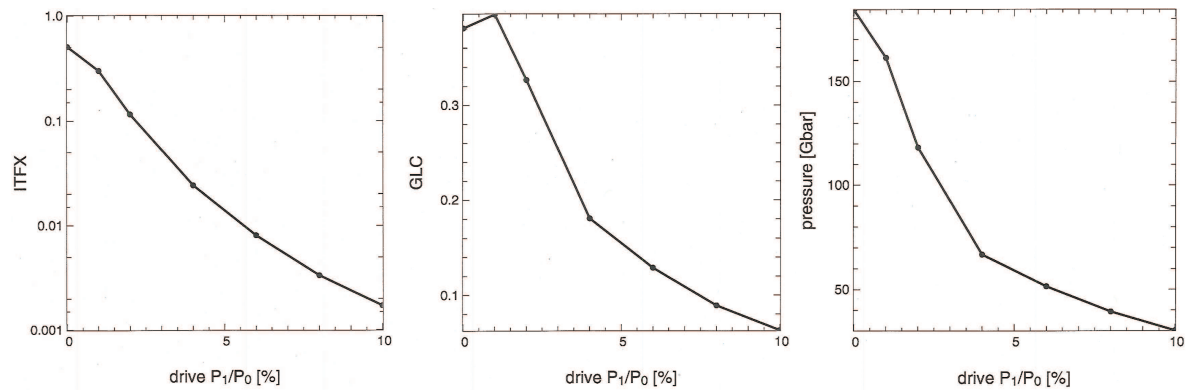
Figure IV.5: ignition performance metrics vs applied P_1 drive perturbation. The ITFX, the GLC, and the hot spot pressure suffer serious reduction as the amplitude is increased. The sensitivity of these metrics to this failure mode suggests that mode 1 asymmetry must be well diagnosed and controlled for ignition experiments.

Milovich, O. S. Jones, P. A. Michel, C. A. Thomas, R. E. Olson, S. Pollaine, R. P. J. Town, S. Haan, D. Callahan, D. Clark, J. Edwards, J. L. Kline, S. Dixit, M. B. Schneider, E. L. Dewald, K. Widmann, J. D. Moody, T. Doeppner, H. B. Radousky, A. Throop, D. Kalantar, P. DiNicola, A. Nikroo, J. J. Kroll, A. V. Hamza, J. B. Horner, S. D. Bhandarkar, E. Dzenitis, E. Alger, E. Giraldez, C. Castro, K. Moreno, C. Haynam, K. N. LaFortune, C. Widmayer, M. Shaw, K. Jancaitis, T. Parham, D. M. Holunga, C. F. Walters, B. Haid, E. R. Mapoles, J. Sater, C. R. Gibson, T. Malsbury, J. Fair, D. Trummer, K. R. Coffee, B. Burr, L. V. Berzins, C. Choate, S. J. Brereton, S. Azevedo, H. Chandrasekaran, D. C. Eder, N. D. Masters, A. C. Fisher, P. A. Sterne, B. K. Young, O. L. Landen, B. M. Van Wonterghem, B. J. MacGowan, J. Atherton, J. D. Lindl, D. D. Meyerhofer, and E. Moses, PHYSICS OF PLASMAS **19**, (2012).